White Rose Research Online

eprints@whiterose.ac.uk
https://eprints.whiterose.ac.uk
Universities of Leeds, Sheffield and York

Deposited via The University of Sheffield.

White Rose Research Online URL for this paper:
https://eprints.whiterose.ac.uk/id/eprint/194044/

Version: Accepted Version

Article:
Marsavina, L., Sapora, A., Susmel, L. et al. (2023) The application of the Theory of Critical Distances to non-homogeneous materials. Fatigue and Fracture of Engineering Materials and Structures, 46 (4). pp. 1314-1329. ISSN: 8756-758X

https://doi.org/10.1111/ffe.13922

This is the peer reviewed version of the following article: Marsavina, L, Sapora, A, Susmel, L, Taylor, D. The application of the Theory of Critical Distances to nonhomogeneous materials. Fatigue Fract Eng Mater Struct. 2023, which has been published in final form at https://doi.org/10.1111/ffe.13922. This article may be used for non-commercial purposes in accordance with Wiley Terms and Conditions for Use of Self-Archived Versions. This article may not be enhanced, enriched or otherwise transformed into a derivative work, without express permission from Wiley or by statutory rights under applicable legislation. Copyright notices must not be removed, obscured or modified. The article must be linked to Wiley's version of record on Wiley Online Library and any embedding, framing or otherwise making available the article or pages thereof by third parties from platforms, services and websites other than Wiley Online Library must be prohibited.

Reuse
Items deposited in White Rose Research Online are protected by copyright, with all rights reserved unless indicated otherwise. They may be downloaded and/or printed for private study, or other acts as permitted by national copyright laws. The publisher or other rights holders may allow further reproduction and re-use of the full text version. This is indicated by the licence information on the White Rose Research Online record for the item.

Takedown
If you consider content in White Rose Research Online to be in breach of UK law, please notify us by emailing eprints@whiterose.ac.uk including the URL of the record and the reason for the withdrawal request.

UNIVERSITY OF LEEDS
University of Sheffield
UNIVERSITY of York

The application of the Theory of Critical Distances to non-homogeneous materials

L. Marsavina[a], A. Sapora[b], L. Susmel[c], D. Taylor[d]

[a]*University Politehnica Timisoara, Faculty of Mechanical Engineering, Blvd. M. Viteazu, No. 1, Timisoara 300222, Romania*
[b]*Department of Structural, Geotechnical and Building Engineering, Politecnico di Torino, Corso Duca degli Abruzzi 24, 10129 Torino, Italy*
[c]*Department of Civil and Structural Engineering, the University of Sheffield, Mappin Street, Sheffield S1 3JD, UK.*
[d]*Department of Mechanical, Manufacturing and Biomedical Engineering, Trinity College, Dublin, Ireland*

Abstract

The Theory of Critical Distances (TCD) has undoubtedly represented a breakthrough in the brittle failure assessment of engineering materials containing defects, crack or notches. The basic idea on which the simplest formulation of the TCD is based is to evaluate an effective stress at a characteristic distance from the tip of the defect/crack/notch and compare it with an inherent fracture strength. Is the critical distance related to the material (micro) structure? Whereas a correlation was already proved for homogeneous materials, the current attention to non-homogeneous ones has brought the question back to the fore. The goal of the present work is therefore twofold: (i) to extend the use of the TCD, through the simple yet effective Point Method (PM), for the static failure assessment of inhomogeneous materials, such as cellular, biological and additively manufactured (AM) materials; (ii) to look for a correlation between critical distance and internal (micro) structure.

Keywords:TCD, critical distance, Point Method, cellular materials, biological materials, AM materials.

1. Introduction

Solid materials are very strong. Strong atomic bonds (ionic, covalent, metallic) found in metals and ceramics have failure strengths of the order of 10-100GPa, whilst weaker types of bonds (Van der Waals and hydrogen bonds) found in polymers have strengths of the order of 1GPa [1]. In use these materials are rarely if ever exposed to such high stresses, so one would never expect an engineering structure to fail. And yet they do. The explanation lies in the phenomenon of stress concentration. Materials contain defects, from atomic vacancies and

dislocations through inhomogeneous structure up to manufacturing flaws and fatigue cracks. The result is stress inhomogeneity, leading to those phenomena that we call fracture and fatigue. To make things worse, engineering structures are designed with inbuilt stress concentrations: few components can avoid such features as holes, notches, corners, etc.

Thus the work associated with predicting the strength of a structure and anticipating its durability implies, in almost all cases, of assessing the effect of stress concentrations. In modern times, thanks to advanced computational methods such as finite element analysis, we can create accurate descriptions of the stress fields around these geometrical features, but the interpretation of this information has proven to be difficult. Many of the most successful approaches make use of the concept of a material-dependant length scale, i.e. a constant which has the units of length. Together with mechanical parameters such as stress, strain and energy, this length scale allows us to predict the conditions under which cracks will form and grow.

The Theory of Critical Distances (TCD)[2] is an approach falling in this category. It uses a constant known as the critical distance, L. Normally, the value of L is determined by conducting experiments on specimens containing different types of stress concentrators – for example notches having different sharpness – and fitting predictions to the data. This work is conducted within the realm of continuum mechanics, making no reference to the microstructure of the material. The resulting values of L vary from micrometres to millimetres and even larger in rare cases. The value of L for a given material will also be different depending on the failure mode, whether it is, for instance, brittle fracture or high-cycle fatigue.

This paper brings together different experiences gained by using the TCD to model and asses a wide variety of materials and failure modes. The aim is to discuss the relationship between the value of L and the scale and morphology of structural features in the material. All materials have structure at some level, but many materials have large-scale structure which has been purposely introduced, creating a material which can be described as “inhomogenous”. These include engineering materials such as concrete, foam and polymer composites, as well as natural materials such as bone. There is much interest in understanding how these engineering materials achieve their strength and toughness, because we have the capacity to alter their structure and thus potentially to optimise their properties. Natural materials have evolved over millions of years and thus have already developed their structure to the best advantage of the organism concerned, so we may be able to learn from them in creating biomimetic materials.

In this paper, after a brief introduction to the TCD and its mode of use, we present a series of sections, each devoted to a different class of materials. Previous work is reviewed, focussing

on the relationship between the continuum-determined L value and the material's structure. The link between the two is the fracture mechanism at the relevant scale.

2. TCD overview

The Theory of Critical Distances (TCD) performs the static assessment by making use of the linear-elastic stress fields damaging the material in the vicinity of the crack initiation locations[2,3,4]. From a practical point of view, the in-field usage of the TCD is based on an effective stress, σ_{eff}, whose calculation involve a material-dependent length scale parameter. According to the way it is defined, σ_{eff} quantifies the extent of damage associated with the entire linear-elastic stress field acting on the material within a finite size domain. In this setting, this process zone is the local portion of material that controls the global strength of the component being designed. The linear-elastic TCD critical distance (which is treated as a material property) is calculated according to the following well-known definition[2]:

$$L = \frac{1}{\pi}\left(\frac{K_{Ic}}{\sigma_{UTS}}\right)^2 \tag{1}$$

where K_{Ic} is the plane strain fracture toughness, whereas σ_{UTS} is the ultimate tensile strength.

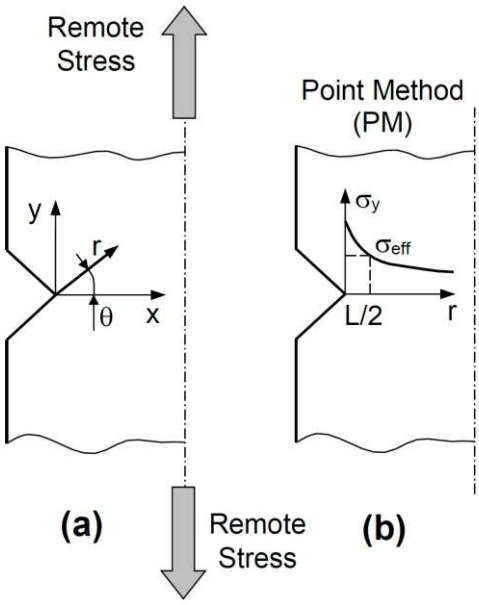

Figure 1: Notch/crack loaded in tension (a) and the TCD used in the form of the PM (b).

While the effective stress can be determined according to different strategies[5], certainly the Point Method (PM) represents the simplest way to use the TCD[2]. The PM is expressed mathematically as follows (Fig. 1):

$$\sigma_{eff} = \sigma_y(\theta = 0, r = L/2) = \sigma_{UTS} \tag{2}$$

In particular, according to Fig. 1b, the PM effective stress coincides with the linear-elastic stress determined at a distance equal to L/2 from the tip of the stress raiser being assessed.

Using the stress field in the vicinity of the notch, other methods can be defined. Considering the average stress instead of the stress function (2), for instance, leads to the well-known Line Method[2]:

$$\frac{1}{2L}\int_0^{2L} \sigma_y(\theta = 0, r)dr = \sigma_{UTS} \tag{3}$$

Similar formulation could be drawn by using the TCD in the form of either the Area or the Volume Method[2].

Furthermore, also energy-based criteria, linking the average release rate of the energy G and comparing it with the fracture energy G_c, were put forward[6,7]. These too are based on a characteristic length depending on L:

$$\frac{1}{1.6L}\int_0^{1.6L} G(a)da = G_c \tag{4}$$

where the factor 1.6 must be replaced by 2 in case of a centre crack.

It is worthwhile also to mention the SED approach[8], which assumes as a critical parameter the strain energy in a small region around the notch tip, whose radius is proportional to L.

The above criteria are generally in good agreement with the PM in terms of failure predictions, and the best accuracy of one method over another varies from case to case.

A somewhat different approach is linked to the coupled Finite Fracture Mechanics (FFM) criterion[9,10], where the stress condition (2) (or (3)) is coupled with the energy balance (4):

$$\begin{cases} \sigma_y(\theta = 0, r = L_{FFM}) = \sigma_{UTS} \\ \dfrac{1}{L_{FFM}} \displaystyle\int_0^{L_{FFM}} G(a)da = G_c \end{cases} \tag{5}$$

In this case, the distance L_{FFM} becomes a structural parameter, depending both on L and on the reference geometry. The advantage of all this is that FFM is able to catch the failure behaviour at small scales[11,12], where, if it were considered a constant length, the method would fail.

In the field of non-homogeneous materials, FFM is here applied to study the scale effect on un-notched concrete[13] and Ultralight-Performance-Fiber-Rinforced-Concrete (UHPFRC)[14] un-notched specimens of width W and subjected to four point bending (FPB). The estimated critical distance L is equal to 8mm for concrete, reflecting microstructural features such as aggregates particles[2], and 47mm for UHPFRC, respectively[15]. In this latter case, the relatively high value of L describes a not very brittle behaviour, and L can be linked to the process zone, as will be clear shortly.

Given the stress field according to classical linear elasticity, and evaluating the energy release rate trough a finite element analysis by ANSYS®code, we were able to solve system (5) and to get the two unknowns: the failure stress σ_f and the critical distance L_{FFM}. Results are plotted in Fig. 2, together with PM predictions.

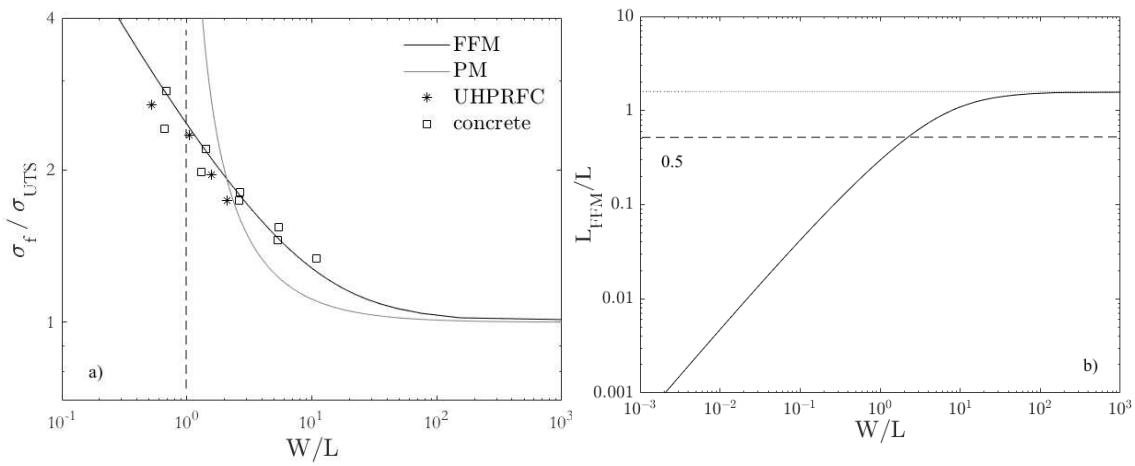

Figure 2: a) FFM and PM failure predictions on experimental data referring to FPB plain samples of width W[13,14]; b) FFM critical distance (in this case, the dashed line refers to PM length L/2).

It can be seen how, as W/L decreases and tends to the unitary value (dashed line, Fig. 2a), the failure load according to the PM diverges, W/2 representing the value according to which the

stress vanishes for a geometry under pure bending. On the other hand, FFM allows a correct description of σ_f even at small scales, with a critical distance L_{FFM} that decreases (with unitary slope) as the scale W decreases (Fig. 2b).

The FFM approach (5) was recently corroborated by showing that failure load estimates are very close to those provided by the well-established Cohesive Crack Model[16,17,18] , once a rectangular cohesive law (i.e. of Dugdale-type[19]) is implemented. The process zone length has a qualitative behaviour similar to $L_{FFM,}$ the two quantities thus being correlated with each other.

Given the above, since the PM is not only very simple to use, but also very accurate, the reliability of the TCD in assessing static strength of inhomogeneous materials will be investigated by considering solely this formalisation of the theory.

Finally, let us underline that an important feature of the TCD is that the same theoretical framework can be used to assess the detrimental effect not only of notches (i.e., finite radius stress raisers), but also of cracks. If attention is focused then on a cracked infinite plate loaded in tension, static strength can directly be estimated by using the PM rewritten as[2]:

$$\sigma_f = \sigma_{UTS}\sqrt{1-\left(\frac{a}{a+L/2}\right)^2} \tag{6}$$

where a is the semi-crack length. Eq. (6) is derived by using the analytical solution formulated by Westergaard[20] to model the stress distribution in the crack tip region of a cracked plate loaded in tension. One of the most relevant peculiarities of Eq. (6) is that, in a very simple and direct way, it is capable of accurately assessing static strength not only in the long-, but also in the short-crack regime, with its usage resulting in a gradual transition from a regime to the other one[2].

3. Cellular materials

Cellular materials (also called foams) are made of interconnected networks of solid struts and cell walls incorporating voids with entrapped gas, resulting in a cellular structure with open (the solid material is found in the edges of the cells), closed (the solid material is found in both the edges and faces of the cells) or mixed (partially open, partially closed) cells. Different

classes of solid materials are used to produce cellular materials like polymers, metals and ceramics.

Their main characteristics are lightweight, high porosity, good energy absorption capacity and floatability. Most cellular materials crush progressively in compression until they reach full densification. In contrast, a brittle fracture behaviour is observed in tension and in presence of cracks and notches[21,22].

The properties of cellular materials depend on those of the solid material from which they are produced, on the relative density (density of the foam divided to density of solid material) and on cell topology (shapes, dimensions) - see Fig. 3 after Ashby (2006)[23]. For sake of clarity, all properties referring to foams will be herein denoted by the superscript *.

Micromechanical models allow the prediction of the mechanical properties of cellular materials based on the properties of solid material from the cell edges (density of solid material ρ_s, Young's modulus E_s, yield stress σ_{ys}), density of cellular material ρ^* and some cellular topology characteristics: length or diameter of cells l and cell wall thickness t [24,25].

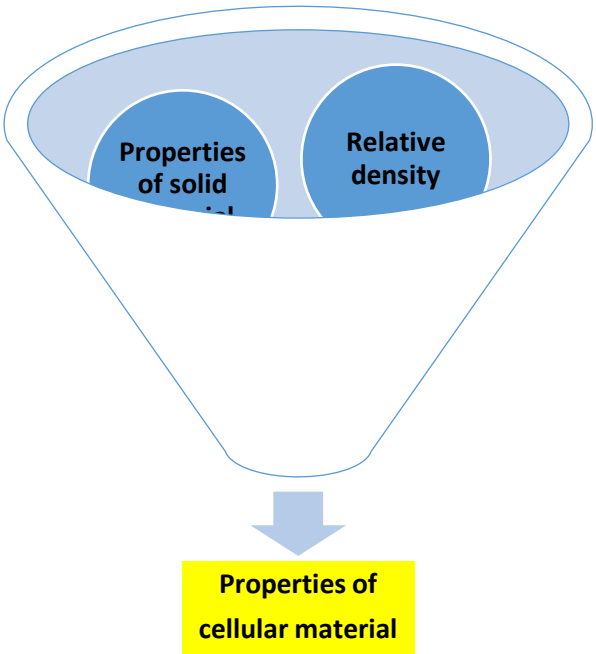

Figure 3: Main parameters influencing the properties of cellular materials.

3.1 Brittle metallic foam

Marsavina et al. (2016)[26] investigated the fracture of brittle aluminium alloy foams AlSi12Mg0.6, produced using powder metallurgical route, where 0.4 wt.% of titanium hydride was employed as foaming agent (Alulight). The chemical composition was Al with 12 wt. % Si and 0.6 wt. % Mg having variable porosity and pore size, and a density between 340 and 1100 kg/m^3 (Fig. 4a). In order to investigate the notch influence under tensile loading (Fig. 4b), specimens having width W = 20±0.6 mm and thickness B = 5±1 mm were machined with circular holes (diameters D = 2.5, 5, 7.5 and 10 mm) and a round U-notch (radius R = 2 mm). For each type of notch, four tests were carried on at room temperature, in displacement control with a loading rate of 2 mm/min on a Zwick/Roell Z005 testing machine.

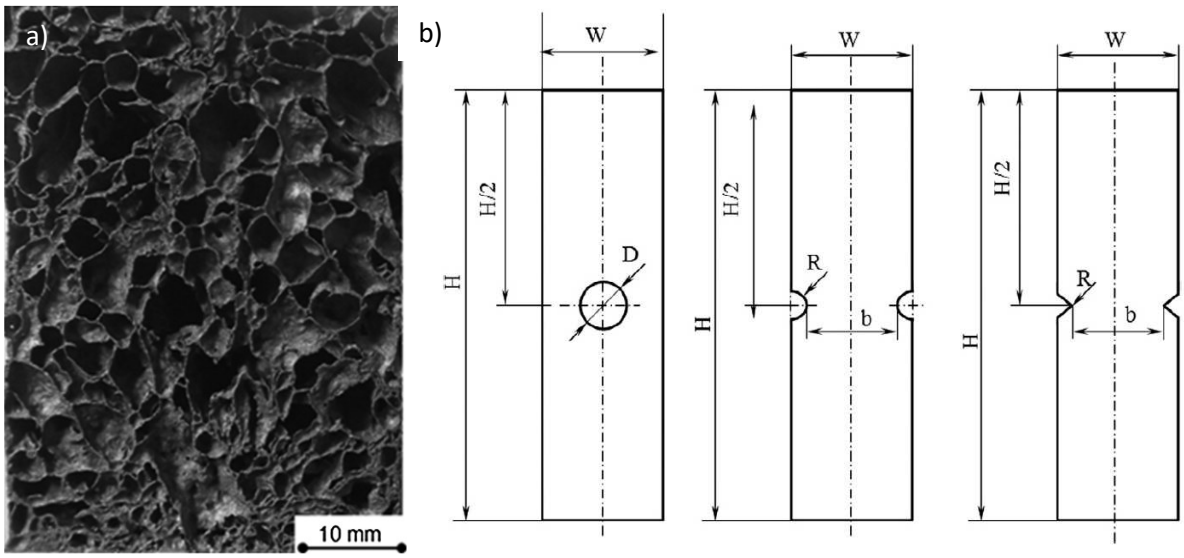

Figure 4: a) Typical microstructure of AlSi12Mg0.6 foam; b) investigated notched geometries.

The critical length for brittle metallic foams, according to Eq. (1), is expressed based on micromechanical models in the form:

$$L = \frac{1}{\pi}\left(\frac{K^*_{Ic}}{\sigma^*_{UTS}}\right)^2 = \frac{c_3^2\left(\rho^*/\rho_s\right)^3 l}{c_0^2 c_2^2\left[c_1\left(\rho^*/\rho_s\right)^{3/2} + c_1'\left(\rho^*/\rho_s\right)\right]^2} \tag{7}$$

where the fracture toughness of the foam is related to the yield stress of the solid material σ_{ys}, cell size l and relative density ρ^*/ρ_s

$$K_{Ic}^* = c_3 \sigma_{ys} \sqrt{\pi l} \left(\rho^* / \rho_s \right)^{3/2} \tag{8}$$

and the tensile strength of the foam can be expressed as:

$$\sigma_{UTS}^* = c_0 c_2 \sigma_{ys} \left[c_1 \left(\rho^* / \rho_s \right)^{3/2} + c_1' \left(\rho^* / \rho_s \right) \right] \tag{9}$$

The critical distance for metallic foams L, Eq. (7), could be thus interpreted as a combination of two factors: the relative density ρ^*/ρ_s and the cell dimension l. Coefficients c_i in Eqs. (7-9) represent some fitting parameters, whose values are provided in Table 1[24].

Table 1. Fitting parameters for brittle metallic foam AlSi12Mg0.6.

Parameter	c_0	c_1	c_1'	c_2	c_3
Value	0.1 - 1.0	0.5	0.3	1.1 - 1.4	0.65

A comparison between the load predicted through the PM (Eq. (2)) and the mean value of the experimental maximum loads is presented in Table 2, together with the structural parameters of the metallic foam and TCD parameters determined with Eqs. (8) and (9). The relative error between the predicted and experimental load is generally below 3% except for the smallest hole, where is around 16%. A very good prediction based on PM could be then evicted.

Table 2. Comparison between predicted loads using PM and experimental maximum loads for aluminium foam specimens.

Notch type	Foam density ρ^* [kg/m^3]	Cell size l [mm]	Critical length L [mm]	Tensile strength σ_{UTS}^* [MPa]	Predicted load F_{pred} [N]	Experimental load F_{exp} [N]	Relative error ε [%]
Hole ϕ2.5	585.9	0.683	1.514	8.32	566.16	487.16	16.2
Hole ϕ5.0	938.5	0.426	0.599	14.88	458.79	452.28	1.44

Hole ϕ7.5	580.5	0.689	1.541	8.23	444.37	437.91	1.47
Hole ϕ10	642.9	0.622	1.264	9.32	365.76	354.69	3.12
U-notch Radius 2	990.9	0.404	0.538	15.93	560.71	550.77	1.80

3.2 Polyurethane foam

Negru et al. (2015)[27] applied the TCD to predict fracture of polyurethane cracked and notched foam components of different densities (100, 145, 300 and 708 Kg/m^3), Fig. 5.

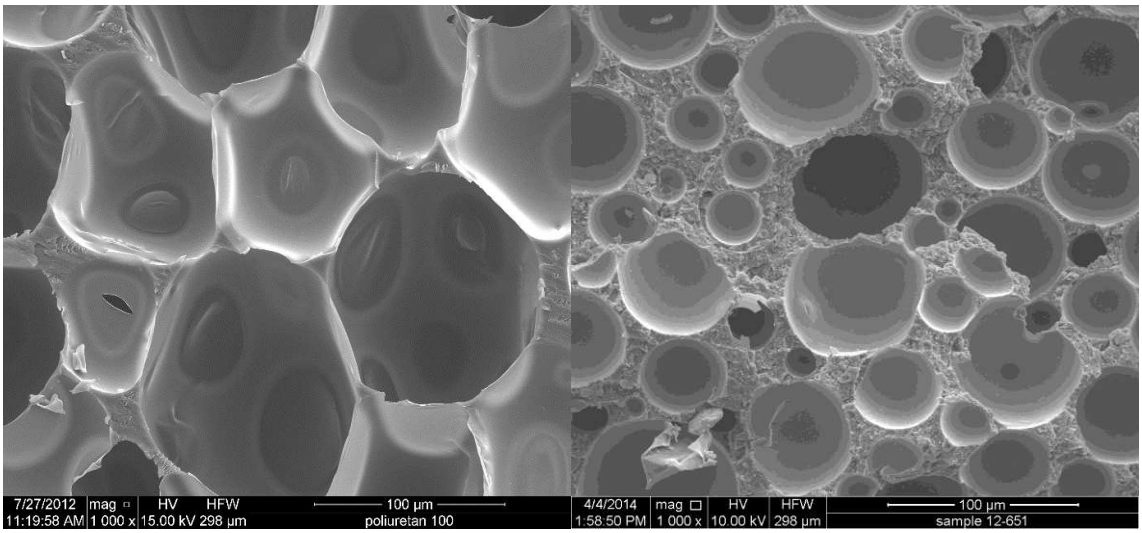

a) 100 kg/m^3 b) 145 kg/m^3

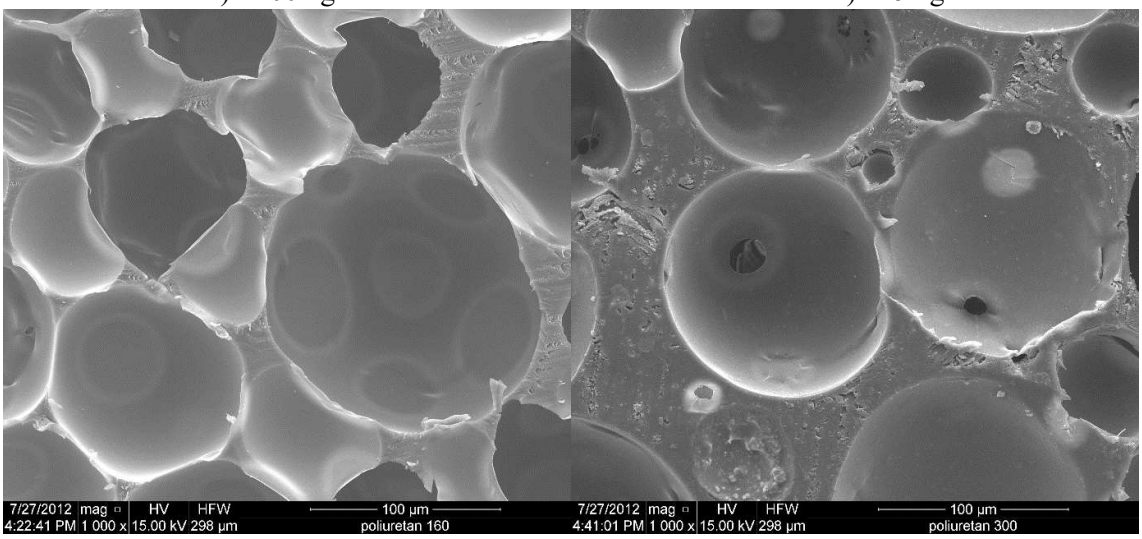

c) 300 kg/m^3 d) 708 kg/m^3

Figure 5: Microstructure of the investigated foams with different densities.

The considered densities span from foam (with very small cell wall thickness) at low densities to a porous solid at high densities. Applying the PM procedure (Eq. (2)), a linear relation between the critical length L to the cell diameter l was proposed (in mm):

$$L = a l + b \tag{10}$$

with a = 5.1 and b = 0.263. Accordingly, L falls in region 0.5-0.8mm, from the highest to the lowest density. In the same study, the inherent stress was linked to the ultimate tensile strength of the polyurethane foam in the form:

$$\sigma_0 = 1.715\sigma^*_{UTS} \tag{11}$$

The TCD parameters were determined from geometries with circular holes and V-notches (similar to those depicted in Fig. 4b), and then applied to U-notched geometries. The use of PM results in very accurate predictions. Indeed, the maximum relative error is found to fall in the range of ± 16%[27,28], Table 3.

Table 3. Comparison between predicted loads using PM and experimental maximum loads for U-notched PUR foam specimens.

Notch type	Foam density ρ^* [kg/m^3]	Cell size l [mm]	Critical length L [mm]	Inherent stress σ_0 [MPa]	Predicted load F_{pred} [N]	Experimental load F_{exp} [N]	Relative error ε [%]
U-notch	100	0.1045	0.79	2.32	224.8	196.0	14.7
	145	0.0838	0.71	3.08	288.38	262.63	9.80
	300	0.0685	0.594	6.02	535.58	462.52	15.8
	708	0.0491	0.518	24.05	2066.15	2139.86	–3.40

4 Biological materials

Biological materials which have a structural, load-bearing role are many and varied, including materials in the bodies of humans and other vertebrates (e.g. bone, cartilage), exoskeletons in arthropods (e.g. insect wings, crab limbs) and the varied support structures of plants, from tree trunks to blades of grass. As a general rule they are fibrous, and therefore usually anisotropic, and are characterised by low fracture toughness in comparison to their strength. Failure almost always occurs by cracking, as evidenced by the brittle fracture of bones, splitting of wood and the microscopic cracks in cartilage which give rise to the painful condition known as arthritis. Given that biological materials fail by cracking, they should be ideal candidates for study using the TCD. Here we present two examples of such work, applying the TCD to bone and to the material in the wings of insects.

4.1 Bone

An initial TCD investigation of bone was carried out[29] using data from the published literature, in which several researchers had measured the effect of holes and cracks of different sizes on the strength of whole bones and of testpieces made from cortical bone. Reasonably accurate predictions (given the scatter in the original data) were achieved with a critical distance value of L = 0.38mm.

How does this distance relate to the structure of bone and the mechanisms of crack growth in it? Toughening mechanisms in bone have been investigated in some detail by Ritchie and others[30,31]. Figure 6 shows a summary of possible toughening mechanisms, which emphasises the fact that bone, as a material, has structure on many different scales, from the macro to nano levels. The value of L which we obtained suggests a mechanism at the larger end of the scale. Bone contains cylindrical structures known as osteons, typically 0.2mm in diameter with a spacing between them of about 0.1mm. There is evidence that these act as barriers to crack propagation: cracks tend to arrest and deflect around the osteon rather than passing through it, as shown in Fig. 7. Unbroken osteons can act as ligaments, spanning between crack faces. So, thanks to the osteons, two toughening mechanisms may arise, referred to as “crack deflection and twist” and “unbroken ligament bridging”. Our L value of 0.38mm is rather larger than the osteon spacing and smaller than the size of a process zone made up of many unbroken osteons. This prompted further analysis, based around the hypothesis that both of these toughening mechanisms could be operating, manifesting themselves at different scales. Experimental evidence for this was found in results on the effect of crack length on measured toughness[30,32]. These two works between them spanned a very wide range of crack lengths, from a few

micrometres to several millimetres. A detailed analysis of these results was carried out, supported by theoretical predictions from model materials having the same toughening mechanisms[33]. It was found that the data could best be explained using two values of L, a smaller value of 0.065mm (which predicted the data from very short cracks) and a larger value of 7.15mm, which predicted the data from longer cracks.

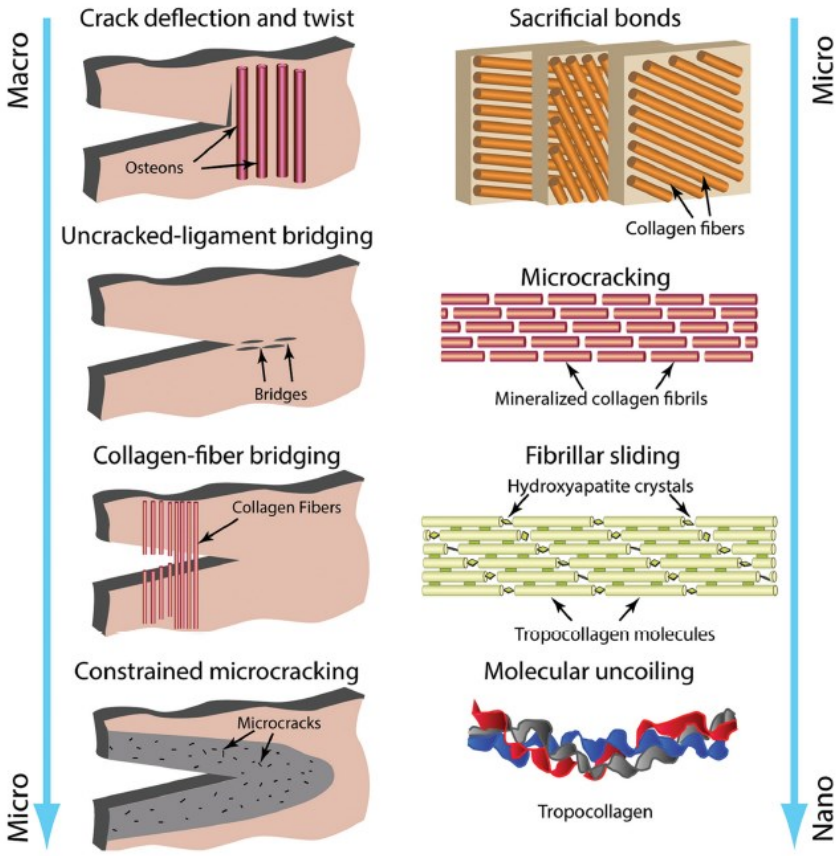

Figure 6: Proposed mechanisms of toughening in bone, from macro to nano scales, from Zimmerman and Ritchie (2015)[34].

The explanation becomes clear: a very short crack, as it grows, will encounter its first osteon when its half-length is of the order of 0.05mm (based on the typical spacing of osteons being 0.1mm). The osteon will be an effective barrier to the crack, giving rise to an L value of similar magnitude. As the crack grows longer these barriers will no longer be significant, instead the major resistance will come from the ligament bridging effect, which involves many individual osteons and thus creates a fracture process zone behind the crack tip of the order of millimetres in length, as observed by previous researchers[30].

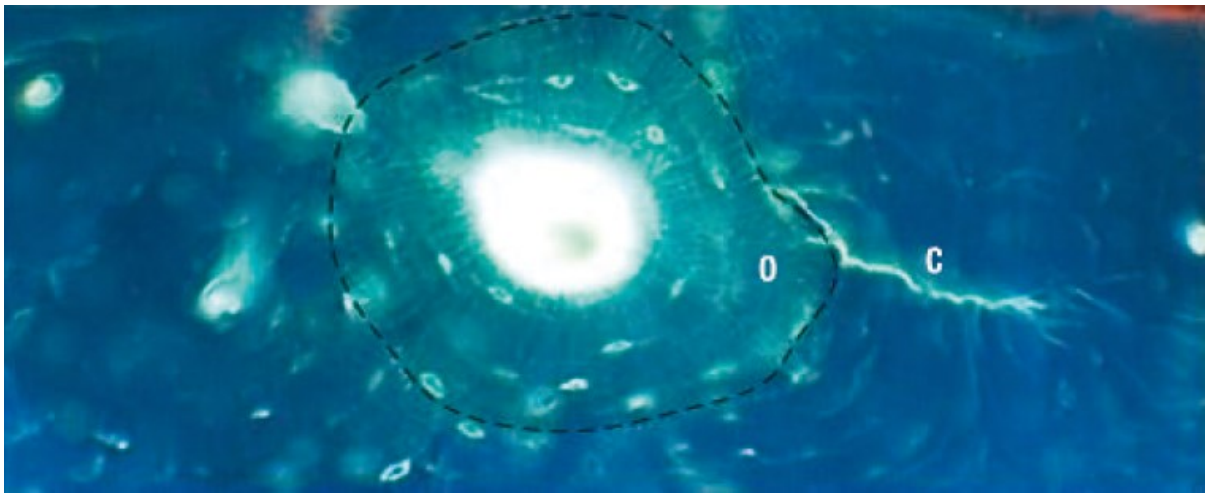

Figure 7: A small crack C (about 0.1mm long) deflected by an osteon O. The outline of the osteon is indicated with a dashed line. Reproduced from O'Brien et al. (2003)[35].

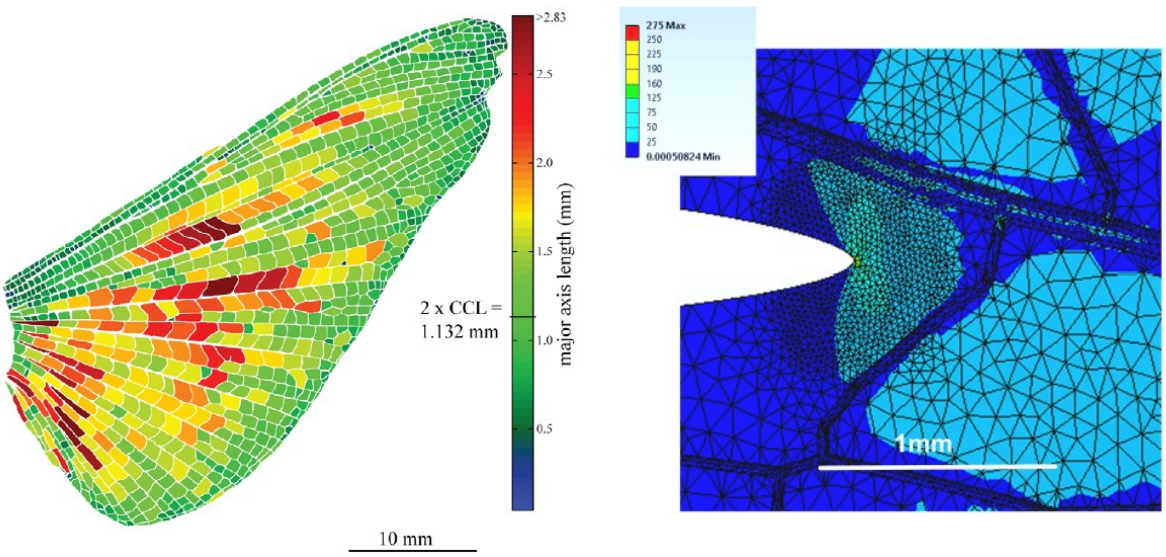

(a) (b)

Figure 8: The insect wing: (a) locust wing with image analysis showing vein separations, from Dirks and Taylor (2012)[36]; (b) finite element model showing crack, membrane and veins, from Schmidt et al. (2020)[37].

4.2 Insect Wing

The wings of insects consist of a thin membrane and a pattern of veins (see Fig. 8a) – thicker, tubular structures which carry the insect's equivalent of blood but also have a structural role. By studying the growth of cracks through the wings of locusts we found that the veins have a toughening effect. Cracks propagating in the membrane arrest at the veins, eventually breaking through if the applied force is increased. This barrier-type toughening mechanism served to increase the toughness of the material by 50%[36].

The spacing of these veins is approximately 1mm, which suggests a critical distance of this order of magnitude. However the membrane material between the veins can be expected to have its own mechanical properties, including L, controlling crack propagation between veins. By conducting tests on microscopic specimens of membrane we established that this material has a tensile strength of 52MPa and a fracture toughness K_{Ic} of 1.19MPa√m. Combining these two values (assuming that the tensile strength is equal to the critical stress s_o) gives an L value of 0.167mm, Eq. (1). By creating finite element models of the exact geometry of the wing, with an introduced crack (see Fig. 8b) we were able to predict the effect of veins with good accuracy using the TCD[37]. The main assumption was that the material in the vein is the same as that in the membrane, so that the only effect of the vein is geometric, a reduction in local stress due to the vein's increased thickness. Thus it emerges that this material also has toughening mechanisms on two different scales, the hundred-micron scale (presumably due to its fibrous structure) and the millimetre scale, determined by the spacing of the veins.

5. Additively manufactured polymers and concrete

The technologies that are most commonly used to additively-manufacture (AM) polymers and concrete make use of an extrusion process where the objects are built layer-by-layer by depositing filaments of the parent material. One of the key features of 3D-printing is that this technology allows objects with intricate designs to be manufactured at a relatively low cost, with this being done by reaching a remarkable level of accuracy in terms of both shape and dimensions. However, the specific features and the intrinsic technological limitations of additive manufacturing result not only in particular material mico-/meso-structural features, but also in defects that are introduced during fabrication. Both material morphology and

manufacturing flaws do affect the overall mechanical behaviour and strength of additively manufactured objects.

In light of the unique features of 3D-printed materials, over the last decade the Sheffield Structural Integrity Research Group has run a number of experimental/theoretical projects to assess whether the TCD is successful in assessing the static[38–43] and fatigue[44–46] strength of notched/flawed 3D-printed materials. In what follows some specific outcomes from this body of systematic research work will be reviewed and revisited by focusing attention specifically on polymers and concrete.

5.1 Notched 3D-printed polymers: in-fill density equal to 100%

Polymers are usually additively manufactured by employing the so-called Fused Deposition Modelling (FDM) technology. This manufacturing process makes use of a heated nozzle that melts filaments of the parent polymer, with these filaments being unwound from a coil. The material that is extruded through the nozzle is deposited directly onto the build plate. By so doing, an initial layer of material is manufactured. When this initial layer is completed, the build plate lowers (or the nozzle moves upward) so that the deposition of the subsequent layer can start. The specific shape of the various layers is obtained by moving the nozzle horizontally. When the filaments forming a layer are deposited, they cool down and harden, with this process allowing the filaments themselves to bind to each other as well to the previous layer of material. Via this technology, an object is built up gradually via a layer-by-layer process. The filaments used to build a layer can be deposited at different angles with respect to the principal axes of the build plate: this angle associated with the printing direction is usually referred to as the raster angle.

As far as both polylactide (PLA) and acrylonitrile butadiene styrene (ABS) are concerned, the mechanical behaviour under static loading of these 3D-printed polymers can be simplified and modelled as follows[38–40]:

- from an engineering point of view, the effect of the manufacturing direction can be neglected, with this resulting just in a little loss of accuracy;
- the mechanical behaviour of additively manufactured PLA and ABS can be modelled via a simple linear-elastic constitutive law.

While the above simplifying assumptions are valid solely for those objects that are 3D-printed flat on the build plate, they apply to materials manufactured with in-fill density set not only equal to 100% [38,40], but also lower than 100% [39].

In order to check the accuracy of the TCD in estimating the static strength of notched PLA as well as of notched ABS, a large number of flat specimens containing different geometrical features were tested under quasi-static tensile loading as well as under quasi-static three-point bending (TPB) [38,40]. The tested samples had all gross width equal to 25 mm, net width to 15 mm and thickness to 4 mm. In order to investigate the effect of the notch sharpness, the specimens were manufactured by making the notch root radius, R, vary in the range 0.05 - 3 mm. Further, both U-notches with opening angle equal to 0° and V-notches with opening angle equal to 135° were considered. All the specimens had thickness of the shell equal to 0.4 mm and were manufactured with an in-fill level equal to 100%. Further, they were fabricated flat on the build-plate by setting the raster angle, θ_r, equal to 0°, 30°, and 45°.

In order to apply the TCD, the critical distance value, Eq. (1), was estimated to be equal to 4.6 mm for PLA[38] and to 4.1 mm for ABS[40]. Despite the simplifying hypotheses being formed to allow the standard TCD to be used, the PM is capable of estimates mainly falling within an error interval of ±20%[38,40]. This is the usual level of accuracy being displayed by the TCD when this approach is used to estimate the static strength of notched/cracked conventionally manufactured engineering materials.

This level of accuracy is certainly satisfactory also in light of the fact that the two 3D-printed polymers being tested were characterised by a very peculiar cracking behaviour (Fig. 9). In particular, the cracks were seen to initiate from the notch tip region, with the initial propagation through the superficial shell occurring on planes experiencing the maximum opening stress - i.e., a Mode I-governed initial growth. After breaking through the shell, the cracks kept propagating along zig-zag paths that followed the directions of the extruded filling filaments (Fig. 9). This complex cracking behaviour was hypothesised to be the result of the combination of three different mechanisms, i.e. (i) de-bonding between adjacent filaments, (ii) de-bonding between adjacent layers and (iii) rectilinear cracking of the extruded filaments [38,40].

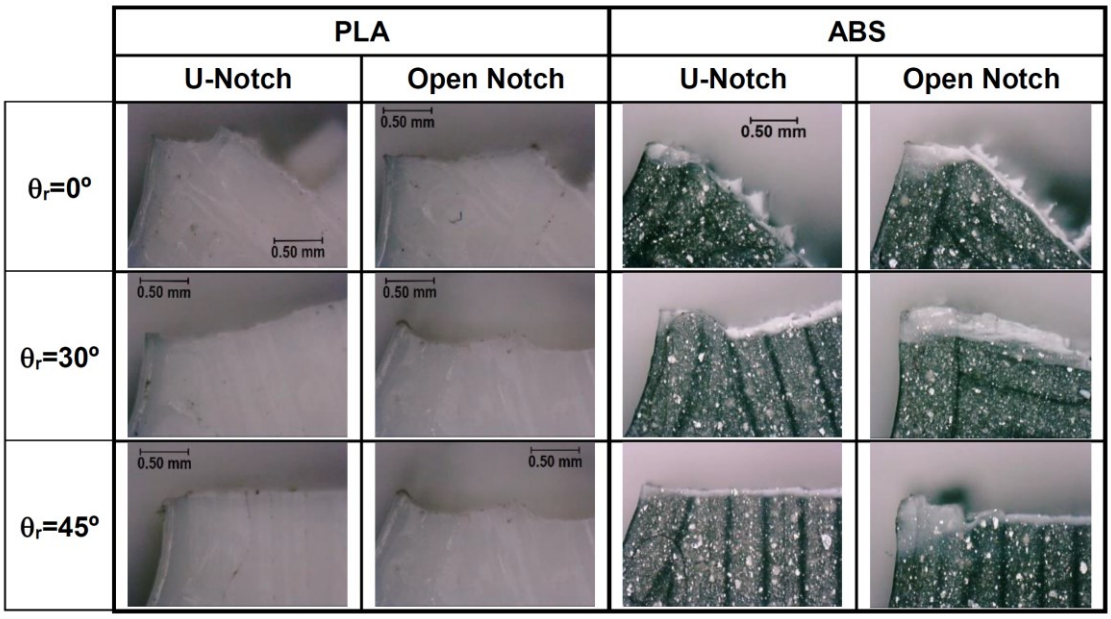

Figure 9: Examples of crack paths observed in notched (R=3 mm) specimens of PLA[38] and of ABS [40] subjected to tensile loading (in the pictures the specimen's longitudinal axis is vertical and the notch tip on the left-hand side).

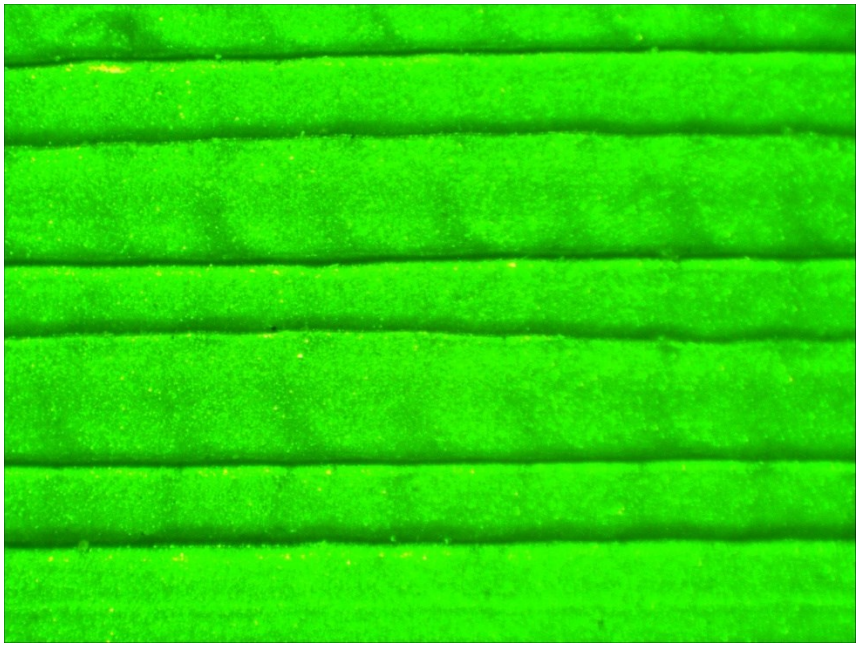

Figure 10: 3D printed PLA structure 100% infill.

As evident from Fig. 10, the components obtained through AM, particularly using the FDM, show an inhomogeneous structure even for the 100% infill.

The critical distance L=4.6 mm estimated by Ahmed and Susmel[38] was also used to predict the fracture load of additive manufactured PLA single edge notch bend (SENB) specimens

obtained via FDM[47,48]. A Prusa MK3 printer was used with the following printing parameters: nozzle diameter 0.4 mm, infill density 100%, nozzle temperature 220° C, bed temperature 60° C, raster angle +45°/–45°, build direction flat through the thickness, and layer thickness 0.15 mm. Three orientations were considered 0°, 45° and 90°. Two type of tests were considered: TPB with span S=4W, and symmetric FPB with span S=4W and distance 2W between the applied loads. For each test and printing orientation, five specimens were tested. A linear elastic finite element analysis was carried on in order to obtain the stress distribution in front of the notch. A polynomial interpolation was performed in order to determine the maximum principal stress at L/2. Considering the inherent stress σ_0 equal to the ultimate tensile strength σ_{UTS} for each printing orientation, the predicted load was determined according to PM. The relative error between predicted loads and the experimental values keeps always within 11%, Table 4.

Table 4. Comparison between predicted loads using PM and experimental maximum loads for SENB specimens made of PLA using FDM technology.

Material	Load Type	Raster angle θ_r [deg.]	Critical length L [mm]	Tensile strength σ_{UTS} [MPa]	Predicted load F_{pred} [N]	Experimental load F_{exp} [N]	Relative error ε [%]
PLA	TPB	0	4.6	50.88	249.50	244.00	2.25
		45		46.77	229.34	220.26	4.12
		90		49.53	242.88	235.17	3.28
	FPB	0	4.6	50.88	499.00	529.77	–5.81
		45		46.77	458.69	515.61	–11.0
		90		49.53	485.76	495.09	–1.88

Summarizing, we can conclude that the critical distance in inhomogeneous/3D printed materials is directly related to the fracture process zone and depends on the microstructural heterogeneity and on the micromechanical material properties.

5.2 3D-printed PLA: different in-fill levels

As far as 3D-printed polymers are concerned, one of the key features of additive manufacturing is that objects can be fabricated by reducing the in-fill level. Setting the in-fill level lower than 100% results in 3D-printed materials having a honeycomb-like internal structure, where the geometrical profile of the structural voids can be changed not only in terms of shape, but also in terms of dimensions. As to the latter aspect, obviously, given the absolute dimensions of the object being manufactured, the size of the manufacturing voids increases as the fill density decreases.

In a similar way, in additively manufactured concrete a combination of both material- and process-related factors can result in manufacturing voids that are introduced during fabrication between adjacent filaments/layers.

The structural voids in 3D-printed polymers are created intentionally to reduce the weight of the objects being manufactured, with this allowing the usage of material to be optimised. In contrast, the fabrication flaws that are seen in 3D-printed concrete are unwanted and their presence is the consequence, on one hand, of the characteristics of the used concrete mix and, on the other hand, of the way the key technological parameters are set.

Independently of their nature (i.e., wanted/unwanted), the voids introduced during manufacturing do affect the overall mechanical properties of 3D-printed polymers and concrete. In this setting, the TCD can be used to model and quantify the effect of internal voids/flaws on the mechanical behaviour and strength of these 3D-printed materials.

To understand the way the TCD can be used to address this problem, initially attention can be focused on the regular internal voids that are intentionally created by setting the in-fill level lower than 100%. Consider then the uniaxially loaded strip of additively manufactured polymer seen in Fig. 11a. The fact that the strip is manufactured by setting the fill density lower than 100% results in regular internal voids having equivalent size equal to d_V. According to Fig. 11a, d_v is taken equal to the diameter of the smallest circle that encloses the void itself [39].

Consider now the infinite plate containing a central through-thickness crack sketched in Fig. 11b and assume that this plate is made of a continuum, homogeneous, isotropic, linear-elastic idealised material. This idealised material is hypothesised to have the same ultimate tensile strength, σ_{UTS}, and the same plane strain fracture toughness, K_{Ic}, as the polymer under consideration when this polymer is 3D-printed with an in-fill level equal to 100%. The semi-length of the central crack, a_{eq}, in the equivalent cracked material is set so that this plate is

assumed to fail under a magnitude of the remote stress equal to the magnitude of the nominal gross stress resulting in the breakage of the additively manufactured strip of Fig. 11a.

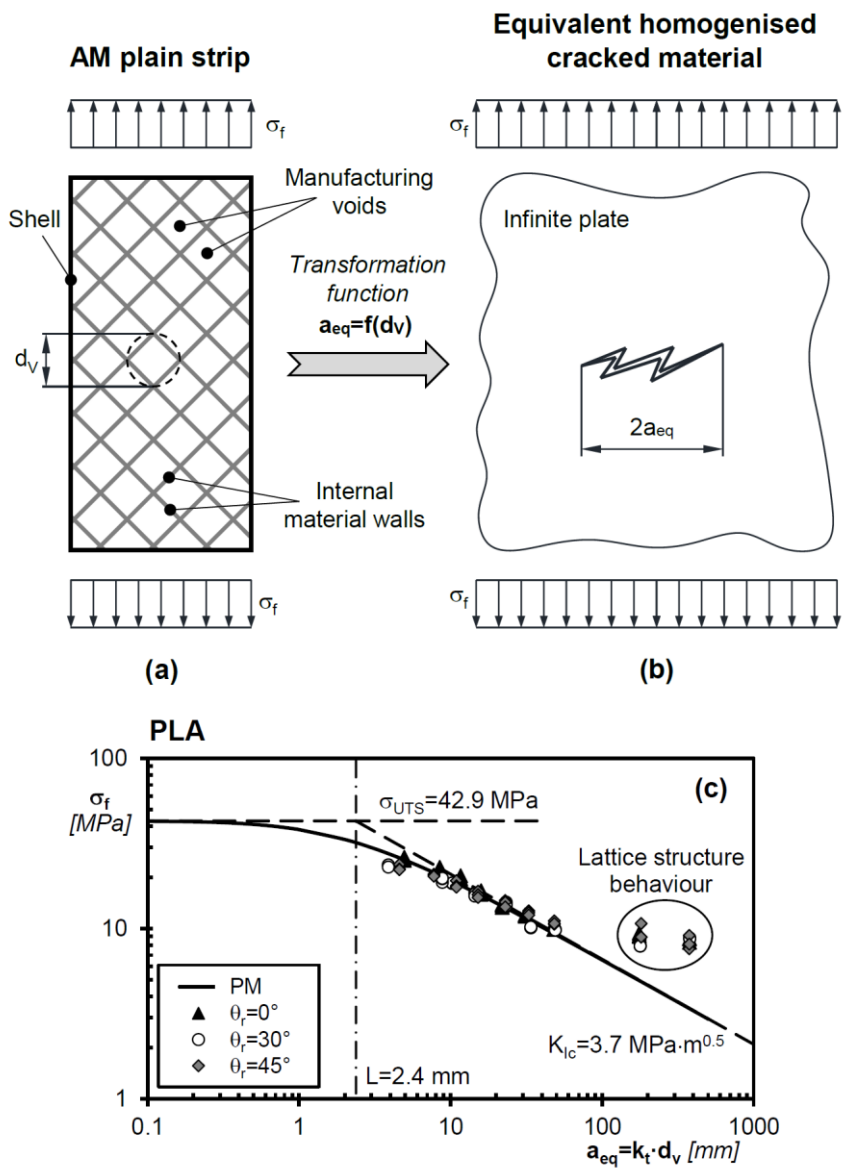

Figure 11: Homogenisation process to turn a plain strip 3D-printed with an in-fill level lower than 100% (a) into an equivalent continuum, homogeneous, isotropic, linear-elastic cracked material (b); accuracy of the PM in estimating the static strength of plain PLA 3D-printed with an in-fill level lower than 100% (c).

As to the homogenised model of Fig. 11b, it is important to point out that the associated LEFM shape factor is invariably equal to unity, with this being an obvious consequence of the fact that the cracked idealised material is modelled as an infinite plate containing a through-thickness central crack.

Having defined the problem according to Fig. 11, the assumption is made that the equivalent semi-crack length, a_{eq}, can be expressed by using a simple linear function [39]:

$$a_{eq} = f(d_v) = k_t d_v \tag{12}$$

where d_v is the equivalent size of the manufacturing voids as defined in Fig. 11a. In contrast, k_t is a dimensionless transformation constant that is used to turn the 3D-printed plain strip of Fig. 11a into the equivalent continuum, homogeneous, isotropic, linear-elastic cracked material of Fig. 11b.

Having transformed the problem of assessing the strength of a 3D-printed material containing voids into a standard LEFM problem involving a crack in an infinite plate, the strength of polymers additively manufactured by setting the in-fill level lower than 100% can be estimated by rewriting Eq. (7) as follows[39]:

$$\sigma_f = \sigma_{UTS}\sqrt{1-\left(\frac{a_{eq}}{a_{eq}+L/2}\right)^2} = \sigma_{UTS}\sqrt{1-\left(\frac{k_t d_v}{k_t d_v + L/2}\right)^2} \tag{13}$$

In Eq. (13), critical distance L is the material length determined for the polymer under consideration when it is manufactured by setting the in-fill level equal 100%. Transformation constant k_t instead can directly be determined from the static strength experimentally determined by testing specimens of the polymer of interest additively manufactured by setting the fill density lower than 100%.

In order to show the accuracy of Eq. (13) in assessing the strength of 3D-printed polymers containing internal manufacturing voids, the Kitagawa–Takahashi diagram of Fig. 11c summarises the results we generated by testing plain specimens of PLA manufactured by making the in-fill level vary in the range 10%-90%[39]. These un-notched specimens were fabricated flat on the build-plate by setting the value of the raster angle, θ_r, equal to 0°, 30°, and 45°. The critical distance value, L, for the investigated PLA 3D-printed with a fill density of 100% was determined to be equal to 2.4 mm (with σ_{UTS}=42.9 MPa and K_{Ic}=3.7 MPa·m$^{1/2}$). From the experimental results generated by testing specimens manufactured with an in-fill level of 80%, the dimensionless transformation constant, k_t, necessary to apply Eq. (13) was estimated to be equal to 35.5[39]. The Kitagawa–Takahashi diagram of Fig. 11c suggests that this simple LEFM/TCD-based idea is successful in modelling the static strength of polymers

additively manufacture by setting the in-fill level lower than 100%. In particular, for the specific material/manufacturing technology used to build the chart of Fig. 11c, it is evident that the use of Eq. (10) returns accurate results down to an in-fill level equal to 30%. In contrast, the behaviour of the specimens manufactured by setting the in-fill level equal to 20% and 10% clearly deviates from the predicted trend. This discrepancy can be ascribed to the well-known fact that a 3D-printed object behaves like a lattice structure when the size of the internal voids is large compared to the absolute dimensions of the object itself. This change in the mechanical response defines the lower limit of the range of validity of Eq. (13). Since the value of this lower limit depends not only on the ratio between object's absolute dimensions and size of voids, but also on a number of different material- and technology-related factors, it should always be determined by running appropriate experiments and/or appropriate numerical simulations.

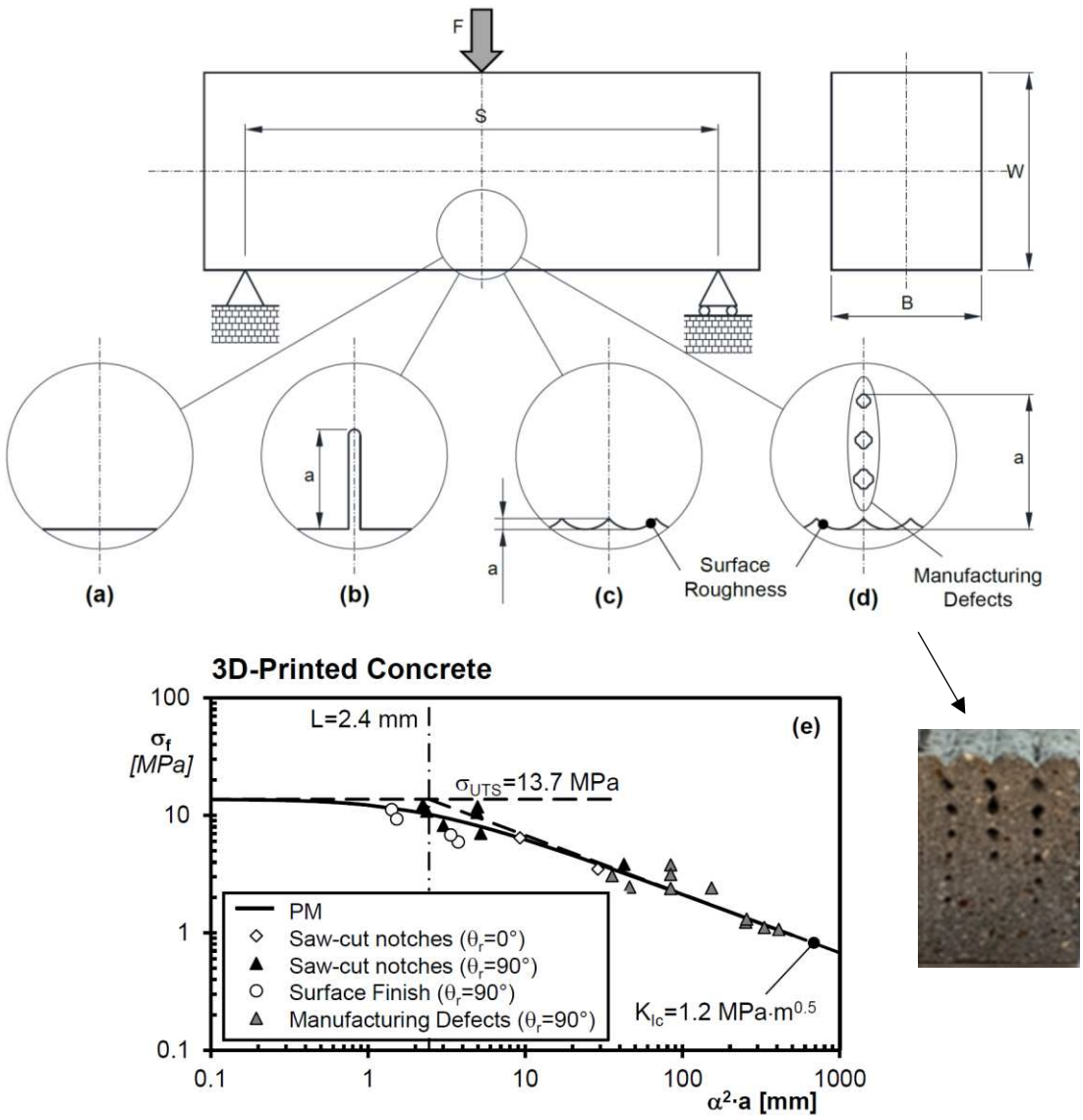

Figure 12: 3D-printed concrete beams loaded in TPB: plain specimen (a); specimen containing a saw-cut crack-like sharp notch (b); specimen weakened by surface roughness (c); specimen weakened by manufacturing defects (d); accuracy of the PM in estimating the static strength of 3D-printed concrete weakened by cracks and defects (e).

Clearly, with regard to AM materials, several papers have been published in the literature based on a critical distance and applied to experimental data[49,50,51], but the conclusions support the results we have shown above.

5.3 3D-printed concrete

Turning to the defects/cracks that can be found in 3D-printed concrete, Figs. 12b to 12d show the possible scenarios that were considered[42] to assess the accuracy of the TCD in addressing this problem. The specimens of 3D-printed concrete being used in this investigation had width, W, in the range 44-53 mm and thickness, B, in the range 34-56 mm (Fig. 12). They were manufactured by setting the raster angle, θ_r, equal to 0° and 90° and tested under quasi-static TPB.

According to Fig. 12, apart from the un-notched specimens (Fig. 11a), samples containing crack-like sharp notches were fabricated by using a circular tip blade with thickness equal to 2.6 mm (Fig. 12b). The depth of these crack-like notches was in the range 2-27 mm. The 3D-printing process was used also to fabricate a number of samples characterised by a very rough surface where this roughness was due to the deposition filaments (Fig. 12c). To assess the strength of these specimens, the valleys characterising the surface were modelled as cracks having depth equal to a (see Fig. 12c). The use of this simple definition for the depth of the superficial roughness-related equivalent cracks returned values of a varying from 1.2 mm up to 3.5 mm. Finally, a number of specimens were additively manufactured by setting the technological parameters so that voids were created intentionally in between adjacent filaments/layers (Fig. 12c). In terms of structural strength modelling, the defects at the fracture section were assumed to be interlinked, resulting in an equivalent crack having length, a, defined as shown in Fig. 12[42].

Taking as a starting point the definitions for the crack depth, a, shown in Figs. 12b to 12d, the Finite Element method was employed to determine the corresponding shape factors, α, where samples were schematised as SENB beams with notch tip radius equal to zero.

Definition (1) was used to determine the critical distance for the 3D-printed concrete under investigation, returning a L value of 2.4 mm. This L value was estimated by taking K_{Ic} equal to 1.2 MPa·m$^{1/2}$ and σ_{UTS} to 13.7 MPa. In particular, the ultimate tensile strength in Eq. (1) was set equal to the static flexural strength of the additively manufacture concrete being tested [42]. The overall accuracy of the PM, Eq. (2), in estimating the static strength of 3D-printed concrete containing the typologies of defects described in Figs. 12b to 12d is summarised in Fig. 12e. In this chart symbol α is used to denote the LEFM shape factor. The Kitagawa–Takahashi diagram of Fig. 12e makes it clear that the use of the TCD can safely be extended also to the static assessment of 3D-printed concrete containing defects and manufacturing flaws.

6. Conclusions

It was shown that, in the framework of TCD, the PM is able to obtain accurate predictions on the failure stress for non-homogeneous materials, both in the presence and in the absence of notches. Three different classes of material were considered: i) foams, both metallic and polyurethane (Section 3); ii) biological materials, with particular reference to the bone and the wing of insects (Section 4); iii) AM polymers and concrete, with different infill levels (Section 5). For all of them, the PM predictions are generally included in an error interval of ±10% with respect to experimental results, and in any case never higher than ±20%.

Finally, it was underlined how, depending on the material, the critical distance L is linked to the material micro-structure. As a matter of fact, in case of foams, L reveals proportional to the size of the cells *l*; for biological materials, L is related to the osteon spacing (bone) or to the vein spacing (insect wing); finally, in AM materials, L depends on the fracture process zone and it is linked somehow to the size of the manufacturing void d_v.

In conclusion, the above examples show that it is possible to use the TCD to predict brittle fracture in inhomogeneous materials. A complicating factor which must be acknowledged is the existence of structure, and important toughening mechanisms, on different scales. However, we can appreciate here a useful role for the TCD in identifying the length scales on which these different mechanisms operate. This can be used in an investigative way when trying to elucidate the operative toughening mechanisms in new materials.

References

1 Ashby MF, Jones DRH. *Engineering Materials 1: An Introduction to Properties, Applications, and Design*. Fourth Edi. Oxford: Elsevier; 2012.

2 Taylor D. *The Theory of Critical Distances: A New Perspective in Fracture Mechanics*. Oxford: Elsevier; 2007.

3 Susmel L, Taylor D. The theory of critical distances to predict static strength of notched brittle components subjected to mixed-mode loading. *Eng Fract Mech*. 2008;75: 534–550.

4 Susmel L, Taylor D. On the use of the Theory of Critical Distances to predict static failures in ductile metallic materials containing different geometrical features. *Eng Fract Mech*. 2008;75: 4410–4421.

5 Bellett D, Taylor D, Marco S, Mazzeo E, Guillois J PT. The fatigue behaviour of three-dimensional stress concentrations. *Int J Fatigue*. 2005;27: 207–221.

6 Pugno NM, Ruoff RS. Quantized fracture mechanics. *Philos Mag*. 2004;84: 2829–2845.

7 Taylor D, Cornetti P, Pugno N. The fracture mechanics of finite crack extension. *Eng Fract Mech*. 2005;72: 1021–1038.

8 Lazzarin P, Zambardi R. A finite-volume-energy based approach to predict the static and fatigue behavior of components with sharp V-shaped notches. *Int J Fract*. 2001;112: 275–298.

9 Leguillon D. Strength or toughness? A criterion for crack onset at a notch. *Eur J Mech A/Solids*. 2002;21: 61–72.

10 Carpinteri A, Cornetti P, Pugno N, Sapora A, Taylor D. A finite fracture mechanics approach to structures with sharp V-notches. *Eng Fract Mech*. 2008;75: 1736–1752.

11 Cornetti P, Pugno N, Carpinteri A, Taylor D. Finite fracture mechanics: A coupled stress and energy failure criterion. *Eng Fract Mech*. 2006;73: 2021–2033.

12 Gallo P, Sapora A. Brittle failure of nanoscale notched silicon cantilevers: A Finite Fracture Mechanics approach. *Appl Sci*. 2020;10.

13 Karihaloo BL, Nallathambi P. Effective crack model for the determination of fracture toughness (KIc) of concrete. *Eng Fract Mech*. 1990;35: 637–645.

14 Lampropoulos A, Nicolaides D, Paschalis S, Tsioulou O. Experimental and Numerical Investigation on the Size Effect of Ultrahigh-Performance Fibre-Reinforced Concrete (UHFRC). *Materials (Basel)*. 2021;14: 5714.

15 Ferrian, F; Cornetti, P; Marsavina, L; Sapora A. Finite Fracture Mechanics and Cohesive Crack Model : Size effects through a unified formulation. *Frat ed Integrità*

Strutt. 2022;61: 496–509.

16 Cornetti P, Sapora A, Carpinteri A. Short cracks and V-notches: Finite Fracture Mechanics vs. Cohesive Crack Model. *Eng Fract Mech*. 2016;168.

17 Cornetti P, Muñoz-Reja M, Sapora A, Carpinteri A. Finite fracture mechanics and cohesive crack model: Weight functions vs. cohesive laws. *Int J Solids Struct*. 2019;156–157.

18 Doitrand A, Estevez R, Leguillon D. Comparison between cohesive zone and coupled criterion modeling of crack initiation in rhombus hole specimens under quasi-static compression. *Theor Appl Fract Mech*. 2019;99: 51–59.

19 Dugdale DS. Yielding of steel sheets containing slits. *J Mech Phys Solids*. 1960;8: 100–104.

20 Westergaard HM. Bearing Pressures and Cracks: Bearing Pressures Through a Slightly Waved Surface or Through a Nearly Flat Part of a Cylinder, and Related Problems of Cracks. *J Appl Mech*. 1939;6: A49–A53.

21 Marsavina L. Fracture Mechanics of Cellular Solids. In: *CISM International Centre for Mechanical Sciences*. ; 2010:1–46.

22 Marsavina L, Constantinescu DM. Failure and Damage in Cellular Materials. In: *CISM International Centre for Mechanical Sciences*. ; 2015:119–190.

23 Ashby MF. Cellular Solids - Scaling of Properties. In: *Cellular Ceramics*. Weinheim, FRG: Wiley-VCH Verlag GmbH & Co. KGaA; 2006:1–17.

24 Gibson LJ, Ashby MF. *Cellular Solids*. Cambridge University Press; 1997.

25 Marșavina L, Linul E. Fracture toughness of rigid polymeric foams: A review. *Fatigue Fract Eng Mater Struct*. 2020;43: 2483–2514.

26 Marsavina L, Kováčik J, Linul E. Experimental validation of micromechanical models for brittle aluminium alloy foam. *Theor Appl Fract Mech*. 2016;83: 11–18.

27 Negru R, Marsavina L, Voiconi T, Linul E, Filipescu H, Belgiu G. Application of TCD for brittle fracture of notched PUR materials. *Theor Appl Fract Mech*. 2015;80: 87–95.

28 Negru R, Marsavina L, Filipescu H, Căplescu C, Voiconi T. Assessment of brittle fracture for PUR materials using local strain energy density and theory of critical distances. *Theor Appl Fract Mech*. 2015;79: 62–69.

29 Kasiri S, Taylor D. A critical distance study of stress concentrations in bone. *J Biomech*. 2008;41: 603–609.

30 Nalla RK, Kruzic JJ, Kinney JH, Ritchie RO. Effect of aging on the toughness of human cortical bone: evaluation by R-curves. *Bone*. 2004;35: 1240–1246.

31 Vashishth D, Tanner K., Bonfield W. Experimental validation of a microcracking-based toughening mechanism for cortical bone. *J Biomech*. 2003;36: 121–124.

32 Mullins LP, Bruzzi MS, McHugh PE. Measurement of the microstructural fracture toughness of cortical bone using indentation fracture. *J Biomech*. 2007;40: 3285–3288.

33 Taylor D. The Theory of Critical Distances applied to multiscale toughening mechanisms. *Eng Fract Mech*. 2019;209: 392–403.

34 Zimmermann EA, Ritchie RO. Bone as a Structural Material. *Adv Healthc Mater*. 2015;4: 1287–1304.

35 O'Brien FJ, Taylor D, Lee TC. Microcrack accumulation at different intervals during fatigue testing of compact bone. *J Biomech*. 2003;36: 973–980.

36 Dirks J-H, Taylor D. Veins Improve Fracture Toughness of Insect Wings. Buehler MJ, a c. di. *PLoS One*. 2012;7: e43411.

37 Schmidt J, O'Neill M, Dirks J-H, Taylor D. An investigation of crack propagation in an insect wing using the theory of critical distances. *Eng Fract Mech*. 2020;232: 107052.

38 Ahmed AA, Susmel L. A material length scale-based methodology to assess static strength of notched additively manufactured polylactide (PLA). *Fatigue Fract Eng Mater Struct*. 2018;41: 2071–2098.

39 Ahmed AA, Susmel L. Static assessment of plain/notched polylactide (PLA) 3D-printed with different infill levels: Equivalent homogenised material concept and Theory of Critical Distances. *Fatigue Fract Eng Mater Struct*. 2019;42: 883–904.

40 Ng CT, Susmel L. Notch static strength of additively manufactured acrylonitrile butadiene styrene (ABS). *Addit Manuf*. 2020;34: 101212.

41 Seibert P, Susmel L, Berto F, Kästner M, Razavi SMJ. Applicability of strain energy density criterion for fracture prediction of notched PLA specimens produced via fused deposition modeling. *Eng Fract Mech*. 2021;258: 108103.

42 Alanazi N, Kolawole JT, Buswell R, Susmel L. The Theory of Critical Distances to assess the effect of cracks / manufacturing defects on the static strength of 3D-printed concrete. *Eng Fract Mech*. 2022;269: 108563.

43 Tu R, Gitman I, Susmel L. Fuzzy inference system for failure strength estimation of plain and notched 3D-printed polylactide components. *Fatigue Fract Eng Mater Struct*. 2022;45: 1663–1677.

44 Ezeh OH, Susmel L. Fatigue strength of additively manufactured polylactide (PLA): effect of raster angle and non-zero mean stresses. *Int J Fatigue*. 2019;126: 319–326.

45 Ezeh OH, Susmel L. On the notch fatigue strength of additively manufactured polylactide (PLA). *Int J Fatigue*. 2020;136: 105583.

46 Wang Y, Wang W, Susmel L. Constant/variable amplitude multiaxial notch fatigue of additively manufactured AISI 316L. *Int J Fatigue*. 2021;152: 106412.

47 Vălean C, Marșavina L, Mărghitaș M, et al. The effect of crack insertion for FDM printed PLA materials on Mode I and Mode II fracture toughness. *Procedia Struct Integr*. 2020;28: 1134–1139.

48 Marșavina L, Vălean C, Mărghitaș M, et al. Effect of the manufacturing parameters on the tensile and fracture properties of FDM 3D-printed PLA specimens. *Eng Fract Mech*. 2022;274: 108766.

49 Cicero S, Martínez-Mata V, Alonso-Estebanez A, Castanon-Jano L, Arroyo B. Analysis of Notch Effect in 3D-Printed ABS Fracture Specimens Containing U-Notches. *Materials (Basel)*. 2020;13: 4716.

50 Cicero S, Martínez-Mata V, Castanon-Jano L, Alonso-Estebanez A, Arroyo B. Analysis of notch effect in the fracture behaviour of additively manufactured PLA and graphene reinforced PLA. *Theor Appl Fract Mech*. 2021;114: 103032.

51 Shahbaz S, Ayatollahi MR, Petru M, Torabi AR. U-notch fracture in additively manufactured ABS specimens under symmetric three-point bending. *Theor Appl Fract Mech*. 2022;119: 103318.